JOURNAL OF MATERIALS SCIENCE 18 (1983) 2752–2764

A transmission electron microscopy study of hexagonal ice

A. H. FALLS*, S. T. WELLINGHOFF
Department of Chemical Engineering and Materials Science, University of Minnesota, Minneapolis, MN 55455, USA

Y. TALMON
Department of Chemical Engineering, Technion – Israel Institute of Technology, Haifa 32000, Israel

E. L. THOMAS
Department of Polymer Science and Engineering, University of Massachusetts, Amherst, MA 01003, USA

The morphologies of fast-frozen, thin-film samples of pure and dilute solutions of salts and surfactants in hexagonal ice are investigated with transmission electron microscopy. The cold-stage microscopy technique is described briefly and limitations imposed by the equipment and the sample itself are discussed. Ice grains, grain boundaries, dislocations, and stacking faults are imaged before radiolysis from the electron beam can alter their structures. The technique shows that screw dislocations in the ice basal plane are common, in accord with observations from X-ray topography and etch-replication microscopy. It also makes visible nonbasal dislocations in hexagonal ice, including dislocations in first prismatic planes, nonprismatic dislocation loops, and stacking faults on first pyramidal planes; heretofore, these defects have not been confirmed experimentally. Implications of the work for cold-stage microscopy of microstructured fluids are mentioned.

1. Introduction

In recent years, fast-freeze, cold-stage transmission electron microscopy has become a major technique for imaging microstructure in dilute, aqueous structured liquid systems [1–5]. Correctly interpreting the images of these fast-frozen samples requires being aware of possible cooling-induced and electron-beam-induced artifacts that may alter the sample as well as the electron-optic contrast mechanisms that produce the image itself. Because water is often a component of the microstructured fluids important in physiological, biological, and chemical products and processes, it is essential to understand the morphology of ice in order to understand the structures that occur in frozen, hydrated structured fluids such as liquid crystalline phases, vesicular dispersions, polymeric suspensions, micellar solutions, and so-called microemulsions. Knowing the structure of ice is also fundamental to cloud physics and glaciology.

Ice, being a crystalline material, can contain matrix defects such as dislocations and stacking faults. These defects can form in crystals growing imperfectly as water solidifies or can be generated when ice is deformed mechanically. Documenting the internal structure of ice is more important to advancing cold-stage transmission electron microscopy (TEM) of structured liquids than studying the surface morphology of ice with scanning electron microscopy [6, 7]. However, despite

*Present address: Shell Development Company, PO Box 481, Houston, TX 77001, USA.

0022–2461/83 $03.00 + .12

the potential power of TEM in elucidating internal microstructure in solids, there have been few studies of ice. The reasons for this are the difficulty of preparing thin specimens and of creating an environment in the microscope that can accommodate them. Another problem is the sensitivity of ice to an electron beam.

All of these difficulties can be circumvented by examining, with TEM, inert replicas of etched ice crystal surfaces. Indeed, replication methods are successful in identifying and studying etch-pits and etch-tracks from dislocations in ice when the crystal surfaces are carefully prepared and etched. Sinha [8] recently reviewed etch-replication microscopy of ice. Unfortunately, dislocations moving in some ice glide planes do not leave behind the vacancy trails with which etchants react and so not all ice slip systems can be revealed by etching [9]. Moreover, dislocation loops, stacking faults, and twins cannot be imaged by etch-replication microscopy.

Better suited than replication to the study of defects in crystalline materials is direct observation of a thin foil of the specimen in a transmission electron microscope. Under appropriate diffracting conditions, good amplitude contrast can be obtained even from small matrix defects. Selected-area diffraction provides additional structural information.

Since cooling-holders and cold-stages have been developed, several investigators have studied ice directly in a transmission electron microscope. For example, Vertsner and Zhdanov [10] and Dubochet *et al.* [11] studied hexagonal and the nonequilibrium cubic and amorphous types of ice formed by condensing water vapour onto cold substrates in the microscope. Taylor and Glaeser [12] observed crystalline ice formed originally outside the microscope, while Hutchinson *et al.* [13] obtained bright-field micrographs and diffraction patterns from what was purported to be amorphous ice prepared with a fast-freeze, double-film technique [14]. Later, Dubochet and McDowall [15] claimed to have formed amorphous ice by spray-freezing water into liquid propane and liquid ethane.

Unwin and Muguruma [16, 17] investigated the defect structure of various forms of hexagonal ice. Their ice samples were prepared originally outside the microscope but were thinned by heating the sample stage, thereby causing the specimen to sublime, and by irradiating the sample with the electron beam. Although they were able to image dislocations, the most prominent structural features in their samples were cavities, which form during sublimation and radiolysis of ice.

The purpose of this paper is to document the features and defect structures in pure and a few dilute solutions of salt or surfactant in hexagonal ice. In Section 2, the fast-freeze, cold-stage microscopy technique is described briefly. In Section 3, the amorphous, cubic, and hexagonal types of ice, which can be formed *in situ* by condensing water vapour onto cooled substrates in the microscope, are studied with electron diffraction. Electron diffraction studies and bright-field and dark-field microscopy of pure hexagonal ice, formed originally outside the microscope, are presented in Section 4; images of dislocations, dislocation loops, and stacking faults in relatively undamaged ice are featured. Defect structures common in frozen, dilute, aqueous solutions of salt and surfactant and in frozen, hydrated dispersions of particles are recorded in Section 5.

2. Experimental materials and methods

Doubly distilled water used to prepare samples was drawn through a four-stage Millipore cartridge system to remove any remaining particulate, ionic, or dissolved organic contaminants. Its conductivity was less than $1\,\mu S\,cm^{-1}$. It was stored in polyethylene bottles to eliminate leaching of ions, which occurs in glass containers [18]. Sodium chloride was certified ACS from Fisher Scientific and dried immediately before use. The surfactant sodium 4-(1′-heptylnonyl)benzenesulphonate (SHBS) (also called "Texas No. 1"), of molecular weight $404.6\,g\,mol^{-1}$ was obtained from the University of Texas and purified by extractions with chloroform and a 95:5 (v:v) solution of isobutanol and water [18]. TRS 10-80, a commercial surfactant, was used as supplied from the Witco Chemical Corporation.

To obtain ice specimens suitable for transmission electron microscopy, samples are prepared with the double-film technique described by Talmon *et al.* [1]. The idea is to capture a thin layer of water, deposited from a syringe, between polymer film-covered grids and to freeze the assembly by plunging it into boiling nitrogen. Once prepared, frozen specimens are transferred into a cooling holder (EM-100SCH) of a JEOL 100CX electron microscope with a Cold-Stage Transfer Module (CSTM). The design of the CSTM

and modifications to the EM-100SCH have been detailed by Perlov *et al.* [19]. The temperature of ice specimens in this cold-stage is about 100 K [19], with heating from the electron beam being insignificant at low electron dose rates [20, 21].

3. Low temperature, low pressure forms of ice

Depending on its temperature and pressure, ice can exist in eight stable crystalline polymorphs, two metastable crystalline forms, or a metastable amorphous state. Fletcher [9, 22] and Hobbs [23] have comprehensively reviewed research on all forms of ice.

At low temperatures and low pressures, the stable equilibrium form of ice is Ice I_h, which has a hexagonal crystal structure [9]. In Ice I_h, each water molecule is tetrahedrally coordinated to its neighbours through covalent and hydrogen bonds, forming sheets of puckered hexagons that are perpendicular to the c (hexagonal) axis. Ice I_h is geometrically similar to both tridymite, a silica mineral, and würtzite (zinc sulphide). Its unit cell is a prism, the base of which is a rhombus with an included angle of $2\pi/3$. The oxygen atoms in the unit cell are located at $\pm(1/3, 2/3, \bar{1}, z_0)$, and $\pm(2/3, 1/3, \bar{1}, 1/2 + z_0)$, where z_0 is about 1/16 and $(hkil)$ denotes standard hexagonal lattice notation [24]. If z_0 were identically 1/16, each molecule would be exactly tetrahedrally co-ordinated in the lattice.

Although Ice I_h is the stable equilibrium form of ice at pressures below 1 kbar (10^8 Nm^{-2}), metastable cubic and amorphous states can also exist. König [25] appears to have been first to discover the cubic phase of ice, Ice I_c. He found cubic ice could be deposited from water vapour onto substrates maintained at temperatures between -150 and -80° C. Later electron diffraction studies [10, 11, 26–29] and X-ray diffraction work [30, 31] confirmed König's observations but showed that the range of substrate temperatures onto which Ice I_c forms depends on the rate of deposition from the vapour, the type of substrate, and the presence of contaminants. Recently, Dubochet and McDowall [15] and Dubochet *et al.* [11] reported that Ice I_c up to 100 nm thick can be formed by spray-freezing water into melting nitrogen.

The structure of Ice I_c consists of two interpenetrating face-centred-cubic lattices centred at (0, 0, 0) and (1/4, 1/4, 1/4) in the unit cell. Its structure is analogous to that of diamond, silicon, germanium, and the cubic minerals sphalerite and cristobalite. Evidence suggests Ice I_c is metastable with respect to Ice I_h. At temperatures above -120° C, Ice I_c transforms slowly but irreversibly to Ice I_h [31]. Measurements of the latent heat of the Ice I_c to Ice I_h phase transformation indicate that the lattice energy of Ice I_h is about 0.5% lower than that of Ice I_c [32].

Burton and Oliver [33, 34] noted that an amorphous form of ice could be deposited from water vapour onto cold copper rods held at temperatures below about -110° C. Amorphous ice, however, is metastable with respect to Ice I_c. The irreversible transformation of amorphous ice to Ice I_c on polycrystalline silver or glass requires about 2×10^7 sec at -160° C and about 2×10^2 sec at -135° C [31].

Because there is a finite partial pressure of water in an electron microscope, a uniform layer of amorphous ice is always deposited on a substrate maintained below about -135° C. Fig. 1 gives proof. Fig. 1a is an electron diffraction pattern from a dry, room temperature polyimide support film approximately 20 nm thick. Polyimide is an amorphous polymer so that Fig. 1a displays broad halos at about 0.22 and 0.12 nm, corresponding to interference from second-nearest and nearest neighbouring molecules.

Fig. 1b shows the electron diffraction pattern from the same polyimide film after it was cooled to -170° C and left in the electron microscope for 2 h. Fig. 1b features three distinct, broad halos, corresponding to spacings of about 0.37, 0.21 and 0.14 nm, respectively. These spacings compare well with those reported for vitreous ice [10, 31]. That the diffraction pattern in Fig. 1b is indeed from amorphous ice is confirmed by heating the polyimide film to a temperature at which the amorphous ice to Ice I_c phase transformation occurs rapidly. Fig. 1c shows the diffraction pattern from the polyimide film after the cold-stage containing the latter was warmed to about -120° C over a period of 1 h. Sharp rings at 0.37, 0.22 and 0.19 nm have replaced the broad halos of amorphous ice. These spacings correspond to the (1 1 1), (2 2 0) and (3 1 1) reflections of Ice I_c.

A microdensitometer trace of the diffraction pattern in Fig. 1c shows a small intensity maximum at 0.39 nm. This maximum is most likely contributed by a small amount of Ice I_h, which is also present. The concentration of Ice I_h, however,

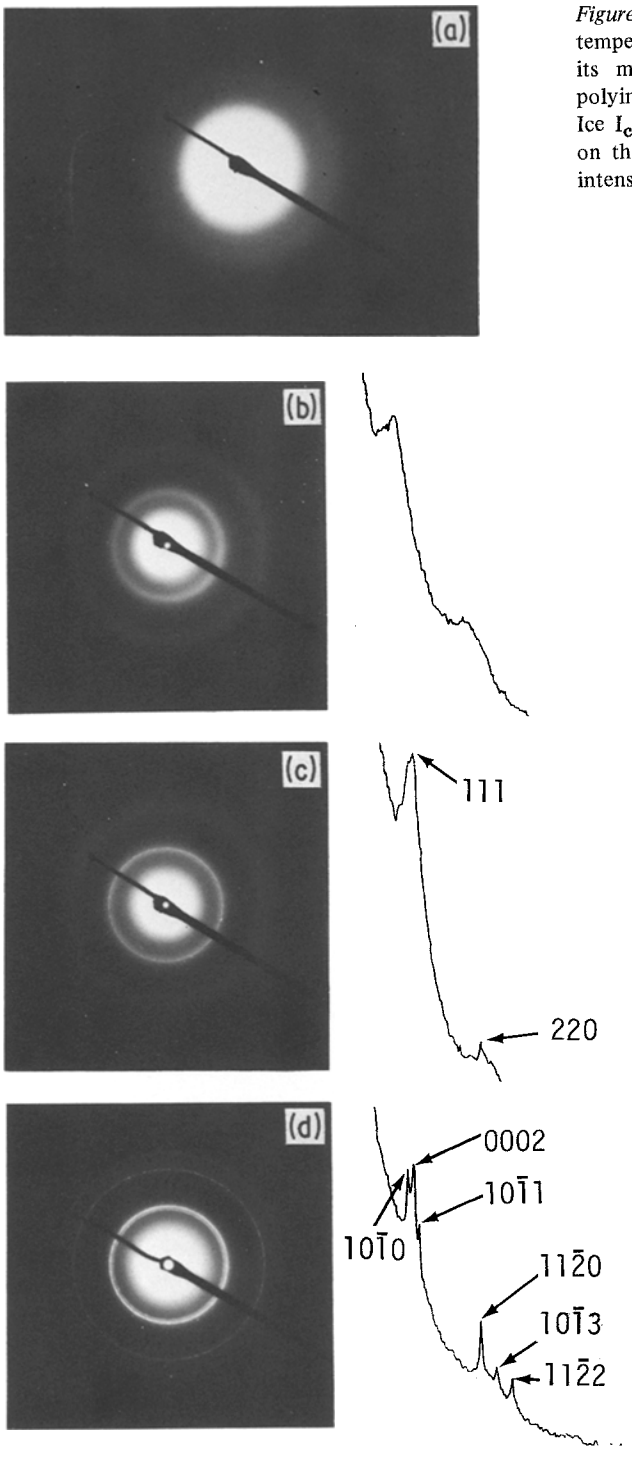

Figure 1 (a) Electron diffraction pattern from a dry, room temperature polyimide film. (b) Scattering pattern, with its microdensitometer trace, from vitreous ice on a polyimide substrate. (c) Electron diffraction pattern from Ice I_c. Distribution of intensities in the pattern is shown on the right. (d) Electron scattering pattern and relative intensities from reflections of Ice I_h.

must be small because the (1 0 $\bar{1}$ 1), (1 0 $\bar{1}$ 2) and (1 0 $\bar{1}$ 3) reflections, which diffract strongly in Ice I_h, are absent in Fig. 1c.

If its temperature is above -120° C, Ice I_c transforms rapidly to Ice I_h. Fig. 1d is an electron diffraction pattern from Ice I_h on a polyimide substrate. The electron diffraction pattern is characterized by three strong reflections at 0.39, 0.37 and 0.34 nm, corresponding to diffraction from the (1 0 $\bar{1}$ 0), (0 0 0 2) and (1 0 $\bar{1}$ 1) crystal planes of Ice I_h.

Fig. 1 may explain the results of Hutchinson *et al.* [13], who claimed to have vitrified water by plunging thin layers of water, between formvar

support films, into melting nitrogen. The amorphous ice diffraction pattern they obtained may have been from ice which deposited from residual water vapour in the microscope onto previously empty areas of the support films. What cannot be explained is why Hutchinson *et al.* saw a direct, rapid transformation of amorphous ice to Ice I_h at -135° C unless the temperature of their sample was higher than -135° C; for Dowell and Rinfret's [31] data show that at -135° C amorphous ice would require more than seven days to transform to Ice I_h and would first transform to Ice I_c!

It has been asserted that bulk water can be vitrified by emulsifying it in n-heptane and jetting the mixture into liquid ethane [35] or by jetting it as a thin layer into a cryomedium [36]. Dubochet and McDowall [15] and Dubochet *et al.* [11] have also reported making amorphous ice up to 1 μm thick by spray-freezing water droplets into liquid propane or liquid ethane. In contrast to Hutchinson *et al.* [13], Dubochet and co-workers back their claims by determining sample thickness. The thickness of their amorphous ice, from differences in the electron beam intensity, measured by mass–thickness contrast, varies in the sample. If amorphous ice is deposited from vapour, its thickness must be more or less uniform. Despite the results published by Dubochet *et al.*, however, there is much doubt as to whether amorphous ice can indeed be formed from the liquid phase [47].

Table I gives the interplanar spacings and relative intensities of the major reflections in the three low temperature forms of ice. The scattering maxima for water are also included to compare with the halos of amorphous ice. The two smaller spacings in amorphous ice coincide with those in water whereas the largest spacing (0.37 nm) differs from the halo centred at 0.32 nm in water. Amorphous ice appears to have a short-ranged structure similar to that of water but to differ in long-ranged order. It may also be more dense than water, as denser materials usually produce larger spacings.

4. Defects in hexagonal ice

When plunged into boiling nitrogen, water prepared with the fast-freeze, double-film technique described by Talmon *et al.* [1] freezes into crystals of Ice I_h. Fig. 2 exemplifies electron diffraction patterns from samples of pure ice and from samples of frozen dilute aqueous solutions. Fig. 2, taken from a 1 wt% aqueous vesicular dispersion of TRS 10-80, displays the $(1\,\bar{2}\,1\,0)$ reciprocal lattice of Ice I_h. All of the diffraction spots in the pattern are Ice I_h reflections (Table I), which proves that the crystal is Ice I_h. The $(0\,0\,0\,1)$ and $(0\,0\,0\,\bar{1})$ diffraction spots are exceptions. These reflections are normally "forbidden" because electrons scattered from the $(0\,0\,0\,1)$ crystal planes interfere destructively. However, if the sample is thick enough, "unallowed" reflections can be produced by double diffraction from "allowed" reflections (e.g. $0\,0\,0\,1$ by $1\,0\,\bar{1}\,0 + \bar{1}\,0\,1\,1$).

Hexagonal ice crystals are not perfect. This section details the defects in thin samples of hexagonal ice as revealed by transmission electron microscopy. The defects examined here grew in freezing layers of water; they were not purposely generated by applying stress.

4.1. Grains and grain boundaries

Frozen sample films are not of uniform thickness. Capillary forces, hydrodynamic forces, and disjoining potential effects all contribute to produce uneven thickness in a draining sample prior to freezing. In areas of the frozen specimen thin enough to be imaged with 100 kV electrons

TABLE I *d*-spacings and intensities of the low-index reflections of low-temperature forms of ice

Hexagonal ice			Cubic ice			Amorphous ice	Water
Hexagonal Miller indices [24], *hkil*	*d*-spacing (nm) [10]	Intensity* (relative)	Miller indices, *hkl*	*d*-spacing (nm) [10]	Intensity* (relative)	*d*-spacing (nm) [10]	*d*-spacing (nm) [10]
$1\,0\,\bar{1}\,0$	0.39	0.65					
$0\,0\,0\,2$	0.367	1	$1\,1\,1$	0.368	1	0.37	
$1\,0\,\bar{1}\,1$	0.344	0.54					
$1\,0\,\bar{1}\,2$	0.267						0.32
$1\,1\,\bar{2}\,0$	0.225	0.55	$2\,2\,0$	0.225	0.33		
$1\,0\,\bar{1}\,3$	0.207	0.26				0.21	0.21
$1\,1\,\bar{2}\,2$	0.192	0.27	$3\,1\,1$	0.192	–		
						0.135	0.135

*This work.

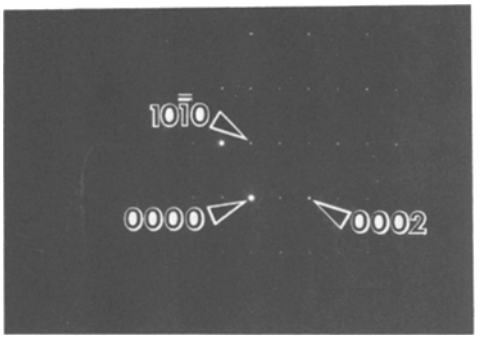

Figure 2 ($1\,\bar{2}\,1\,0$) reciprocal lattice of hexagonal ice in a frozen, 1 wt % aqueous vesicular dispersion of TRS 10-80.

($<\sim 1\,\mu m$ thick), single-crystal ice grains have areas of several square microns. Grain sizes in the sample depend, of course, on the conditions under which the solid phase nucleates. Nucleation is affected by the rate at which the sample is frozen and by the disjoining potential [37] in thin fluid films [38]. Disjoining effects arise because molecules in a thin film reside in an environment which differs from that in a bulk phase at the same temperature and chemical potential. The disjoining potential may also perturb pre-frozen states in samples; this subject is not treated in this paper.

Solutes also affect nucleation in aqueous samples; ice grain sizes diminish as the concentration of solutes or dispersed particles increases.

Boundaries between ice grains in thin samples are almost always perpendicular to the film surface. Figs. 3a and b show a high-angle boundary between two grains of pure, hexagonal ice. In Fig. 3a, the normal to the film surface is parallel to the electron beam. The boundary between the ice grains is fairly sharp and does not display thickness contrast fringes, which would be present if the boundary ran obliquely through the film [39]. When the specimen is tilted 22° to make the boundary oblique to the electron beam (Fig. 3b), fringes are present. Nucleation and growth in a thin film gives grain boundaries perpendicular to the sample surface because the crystal grows quickly across the thickness of the film. Thereafter, it can grow laterally until it contacts another crystal growing from a separate nucleus.

The boundary shown in Fig. 3 is identified as separating two ice grains not only by its appearance but because at it bend contours are discontinuous and because the selected-area diffraction patterns taken from grain I (Fig. 3c) and grain II (Fig. 3e) differ. The pattern from the boundary region (Fig. 3d) has spots originating from both ice grains.

Although grain boundaries orient preferentially, crystallographic directions do not. That is, there is no special alignment of crystal planes in thin ice samples; a given grain can have any orientation.

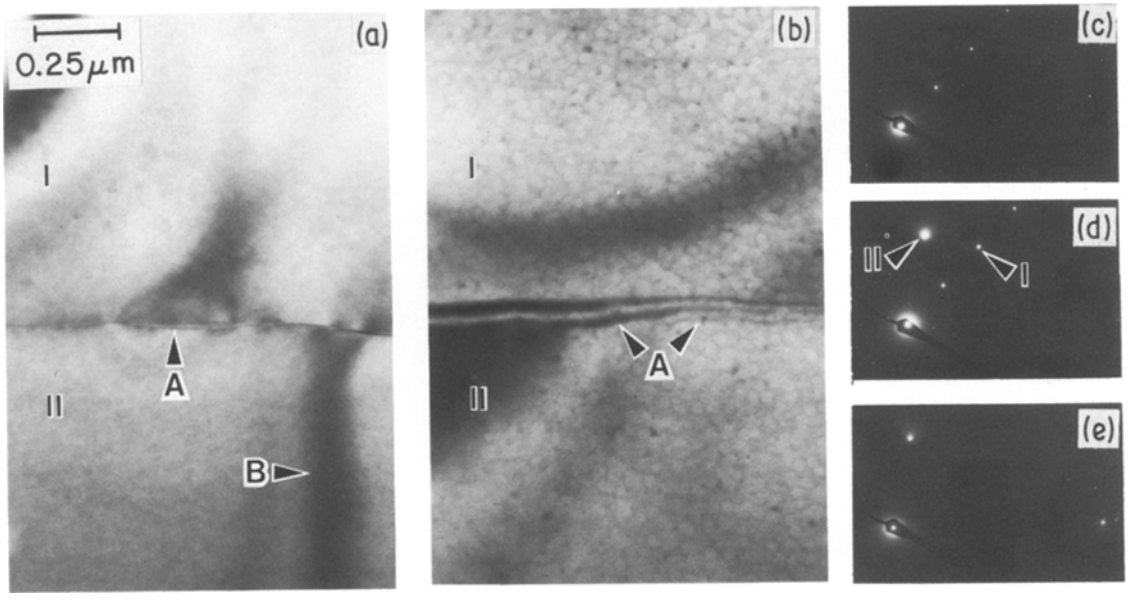

Figure 3 (a) Bright-field micrograph of an untilted grain boundary (A) in ice. The ice grains also display bend contours (B). (b) Same area after 22° of tilt. Thickness fringes have appeared at the grain boundary (A). (c) Selected-area diffraction pattern from uppermost grain (I). (d) Diffraction pattern from grain boundary. Spots from both grains (I and II) are visible. (e) Diffraction pattern from ice grain II.

4.2. Ice slip systems and images of dislocations

Like any other crystalline material, hexagonal ice deforms plastically under stress through the motion of dislocations. Tyson [40] catalogued the slip systems and the elastic strain energies of the dislocations that should theoretically occur in Ice I_h. These slip directions and planes are listed in Table II. Not all have been confirmed experimentally. However, some dislocations in hexagonal ice have been identified by X-ray topography [41, 42]. This technique and etch-replication microscopy have established that screw dislocations, lying in the basal plane with Burger's vectors $a/3\ \langle 1\,1\,\bar{2}\,0\rangle$, are primarily responsible for glide in ice. Prismatic dislocation loops in the basal plane with $c[0\,0\,0\,1]$ Burger's vectors have also been imaged by X-ray topography [43]. Moreover, etch-pits and etch-tracks from nonbasal dislocations have been revealed by etch-replication microscopy [8], but their slip planes cannot be determined with this technique [9].

For imaging dislocations in ice, cold-stage transmission electron microscopy is preferred over both X-ray topography and etch-replication microscopy. With TEM, small defects can be imaged that cannot be resolved by X-ray topography; a stacking fault between two partial dislocations separated by a few tens of nanometres (Fig. 11a) is an example. Fast-freeze sample preparation is less restrictive than etch-replication, which relies on an etchant to remove preferentially ice molecules near a defect. Etch-replication methods are also subject to numerous experimental variables [8].

High-resolution electron microscopy of ice, however, is difficult because cold-stage equipment and the sample itself impose limitations. In room temperature stages, a specimen can be tilted about two separate axes so that particular crystallographic orientations can be made to diffract. In contrast, present cold-stages tilt about just one axis. Grid bars and trap grids, used to shield the specimen from contaminants and thermal radiation [1], can also block diffracted beams when the stage is tilted. Resolution in cold-stages is further limited by mechanical instabilities.

These equipment problems may be overcome in the future. In fact, a cold-stage which permits tilt about two axes has been developed recently by Swann [44]. Unfortunately, radiation damage, which cannot be circumvented, hampers the microscopy of defects in ice. Whereas Burger's vectors of dislocations in metals can be conclusively identified from images formed from many sample orientations, information in ice is limited to but three or four diffracting conditions before radiation damage alters the sample.

Fig. 4 illustrates how radiation damage can intrude before dislocations in ice can be identified. Fig. 4a is a bright-field image of dislocations in pure hexagonal ice. Many dislocations are piled up along a low-angle grain boundary near the top of the figure. Five other dislocations are visible in the right-centre of the figure. If these dislocations belong to the most probable slip system, their Burger's vectors must be of the form $a/3\ \langle 1\,1\,\bar{2}\,0\rangle$. The Burger's vectors can be identified by finding dark-field images in which the dislocations vanish. That is, images for which the projection of the Burger's vector onto the diffraction vector, $\mathbf{b}\cdot\mathbf{g}$, is zero [39].

If the Burger's vector of any of the dislocations in Fig. 4a is $\mathbf{b} = a/3\ [1\,\bar{2}\,1\,0]$, the dislocation should be absent in the $(\bar{3}\,0\,3\,2)$ dark-field image shown in Fig. 4b. It appears, however, that the Burger's vectors of at least four of the dislocations have a component along $(\bar{3}\,0\,3\,2)$. At some places (A) in Fig. 4b, the dislocation takes the local crystal planes closer to diffracting conditions; at other places (B), dislocations take the planes away from reflection. If $\mathbf{g}\cdot\mathbf{b}$ was zero, the dislocation image would disappear into the background matrix.

Rather than vanish in the $(1\,\bar{2}\,1\,\bar{2})$ dark-field image (Fig. 4c), the dislocations produce doubled

TABLE II Ice slip systems [9, 40]

Slip plane	Slip direction, b	Dislocation character	$K\lvert\mathbf{b}\rvert^2$ (10^{-10} J m^{-1}) (proportional to energy of dislocation)
$(0\,0\,0\,2)$	$\langle 1\,1\,\bar{2}\,0\rangle$	screw/edge	6.15/9.85
$(0\,0\,0\,2)$	$\langle 1\,0\,\bar{1}\,0\rangle$	screw/edge (partials)	2.05/3.28
$\{1\,0\,\bar{1}\,0\}$	$\langle 1\,1\,\bar{2}\,0\rangle$	screw/edge	6.15/9.86
$\{1\,0\,\bar{1}\,1\}$	$\langle 1\,1\,\bar{2}\,0\rangle$	screw/edge	6.15/9.76
$\{1\,0\,\bar{1}\,0\}$	$\langle 0\,0\,0\,1\rangle$	screw/edge	15.3/27.3
$\{1\,1\,\bar{2}\,0\}$	$\langle 0\,0\,0\,1\rangle$	screw/edge	15.3/27.3

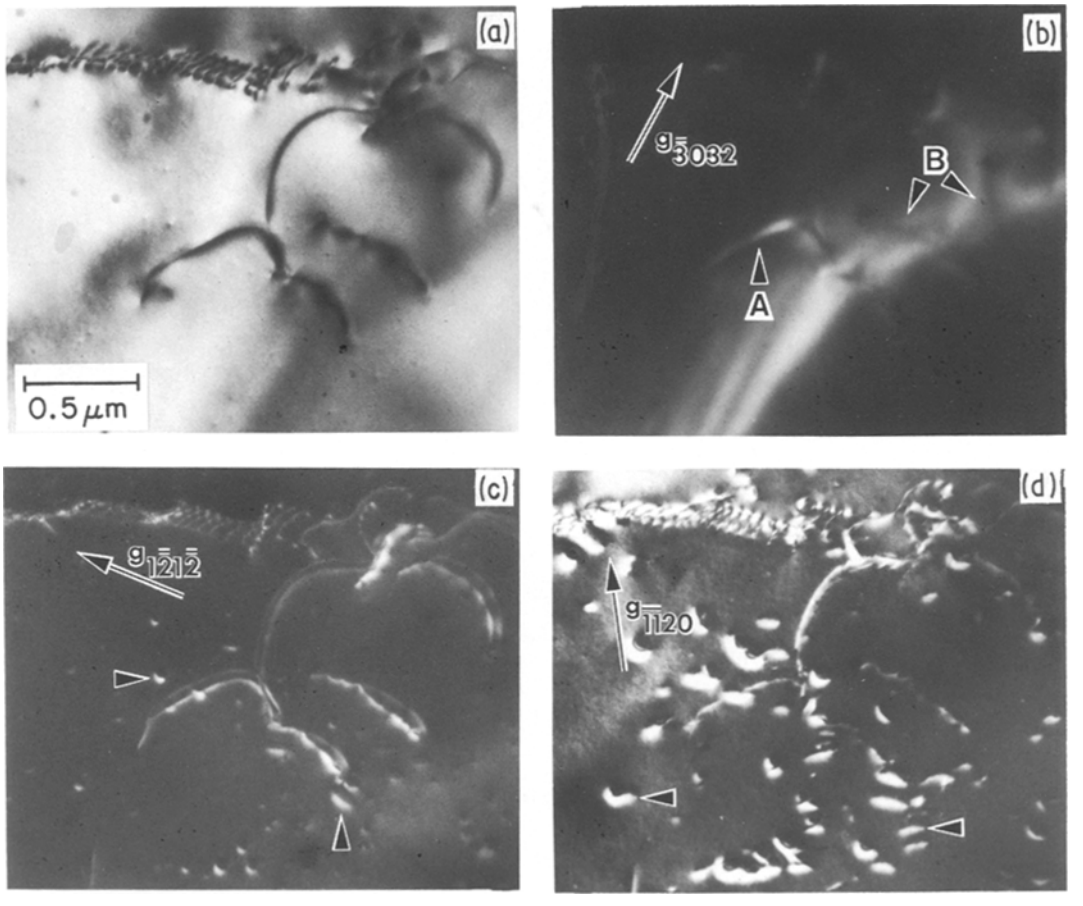

Figure 4 (a) Bright-field micrograph of dislocations in hexagonal ice. Film orientation is $[2\,\bar{2}\,0\,3]$. (b) $(\bar{3}\,0\,3\,2)$ dark-field image of (a). Dislocation lines remain visible. (c) $(1\,\bar{2}\,1\,\bar{2})$ dark-field image. Dislocation lines have doubled images. Radiolysis from the electron beam induces defects in ice (arrows). (d) $(\bar{1}\,\bar{1}\,2\,0)$ dark-field image in which dislocations remain visible. Radiation-induced defects (arrows) have increased in number and strongly diffract electrons.

images. Doubled images indicate that $\mathbf{g} \cdot \mathbf{b}$ is greater than two [39]. Moreover, small areas of positive contrast are visible in Fig. 4c (arrows). These are from defects induced by the electron beam. By the time the third dark-field image of this area is formed (Fig. 4d), radiation-induced defects are more pronounced than the original dislocations!

Because equipment and radiation damage limit the data that can be obtained from ice, dislocations must be identified by assuming that they belong to a probable slip system. By considering all low-index slip systems, the analysis proceeds by trial and error, matching experimental observations of projected directions and angles with those calculated theoretically. This method proves inconclusive if no assigned system is consistent with microscope images. However, if one slip system happens to match the data, it can be assigned to the defect.

4.2.1. Basal dislocations

In cases where slip systems can be identified, cold-stage microscopy reveals $(0\,0\,0\,2)\langle 1\,1\,\bar{2}\,0\rangle$ screw dislocations to be common in hexagonal ice. Fig. 5 shows dislocations in the basal plane of ice. Because they are several microns in length and the film is less than 1 μm thick, these defects must lie in the sample plane, which is $(0\,0\,0\,1)$. Most of the dislocation lines in Fig. 5 are parallel to $[1\,1\,\bar{2}\,0]$ or $[\bar{2}\,1\,1\,0]$ and thus are likely to be $a/3\langle 1\,1\,\bar{2}\,0\rangle$ dislocations of mostly screw character.

4.2.2. Nonbasal dislocations

Although less common, nonbasal dislocations also exist in ice. Fig. 6 is an example. If a dislocation line in the crystal is nearly coplanar with the normals to its slip plane and the sample plane, the slip plane can be identified from the angle it makes

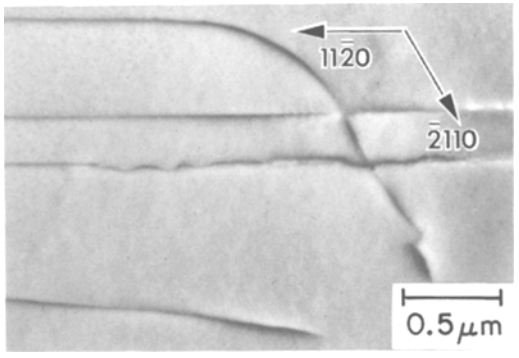

Figure 5 Bright-field image of $a/3\langle 1\,1\,\bar{2}\,0\rangle$ screw dislocations in the ice basal plane.

with the plane of the sample surface. The tangent of this angle is the extinction distance of the operating reflection divided by the distance between thickness fringes in the image. The most probable slip direction can then be assigned and compared to the projected direction of the dislocation line in the image to determine the screw/edge nature of the defect. A large magnitude of the projection of the Burger's vector onto the diffraction vector, $\mathbf{b}\cdot\mathbf{g}$, provides a check on the indexing of the system.

Figs. 6a and b are a $(1\,1\,\bar{2}\,0)$ dark-field/bright-field pair of micrographs taken from an ice crystal near a break in the film. Screw dislocations appear in two slip systems: $(1\,0\,\bar{1}\,0)[1\,\bar{2}\,1\,0]$ and $(0\,\bar{1}\,1\,0)[\bar{2}\,1\,1\,0]$, which heretofore have not been confirmed experimentally. The angle these make with the sample plane is measured as $\tan^{-1}[(\xi_{1\,1\,\bar{2}\,0} = 130\,\text{nm})/57\,\text{nm}] = 66°$; the calculated angle is 65°. The dislocation lines in the figures are about 48° and −38° from $[1\,1\,\bar{2}\,0]$. These angles compare favourably with angles of ± 43°, which are calculated by assuming that the defects are screw dislocations. Moreover, $\mathbf{g}\cdot\mathbf{b} = 1$ for both sets of defects, indicating that they should have about the same contrast in the images.

Fig. 6b also shows cavities that form in ice during radiolysis [17]. These cavities do not appear to interact preferentially with dislocations; other features, e.g. surfaces or grain boundaries, may have more influence on nucleation and growth of radiation-induced cavities in thin films of ice.

Fig. 7, which shows a dislocation in an ice crystal oriented with $[1\,\bar{2}\,1\,0]$ perpendicular to the film surface, is another example of nonbasal dislocations in ice. The dislocation is absent in the $(0\,0\,0\,\bar{2})$ dark-field image (Fig. 7c). Here the matrix is near the exact diffracting condition and the dislocation takes the local crystal planes neither out of nor farther into reflection. Thus $\mathbf{g}\cdot\mathbf{b}$ is zero, indicating that the Burger's vector of this defect does not have a component along the c axis. The most likely displacement vector without a component along the hexagonal axis is of the form $a/3\langle 1\,1\,\bar{2}\,0\rangle$. However, because the dislocation is visible in the $(1\,0\,\bar{1}\,3)$ dark-field image (Fig. 7b), $\mathbf{b}$ cannot be $a/3\,[1\,\bar{2}\,1\,0]$. $\mathbf{b} = a/3\,[1\,1\,\bar{2}\,0]$ or $\mathbf{b} = a/3\,[\bar{2}\,1\,1\,0]$, however, remain possible.

If the dislocation lines in Fig. 7 lie within a single plane, the latter cannot be the basal plane. Basal planes are perpendicular to the $(1\,\bar{2}\,1\,0)$ sample plane. Hence, any dislocation line in $(0\,0\,0\,\bar{2})$ would project as a single line in the images in Fig. 7. Because the dislocation lines are not colinear, they must lie in nonbasal planes, perhaps in first prismatic, $\{1\,0\,\bar{1}\,0\}$, planes.

4.2.3. Dislocation loops

Dislocation loops also exist in hexagonal ice

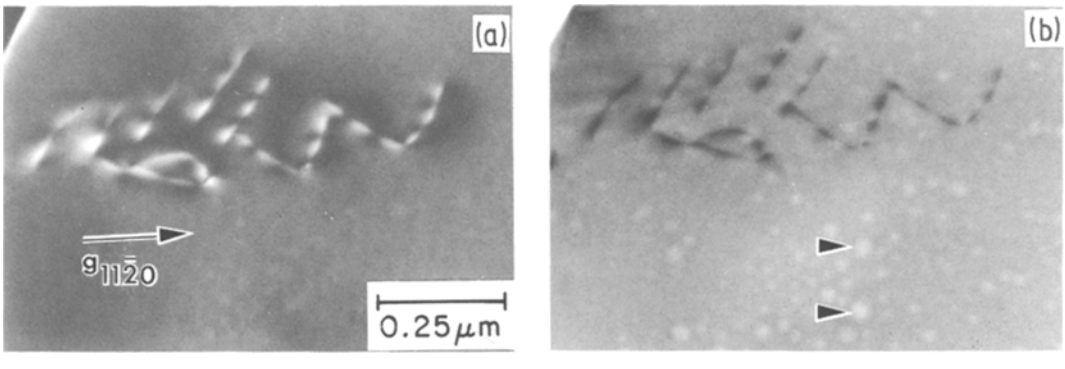

Figure 6 (a) $(1\,1\,\bar{2}\,0)$ dark-field image of dislocations from the $(1\,0\,\bar{1}\,0)[1\,\bar{2}\,1\,0]$ and $(0\,\bar{1}\,1\,0)[\bar{2}\,1\,1\,0]$ slip systems of hexagonal ice. Film orientation: $[3\,\bar{3}\,0\,2]$. (b) Bright-field micrograph of Fig. 6a. Cavities (arrows) formed after the area was exposed to approximately 0.1 C cm^{-2}.

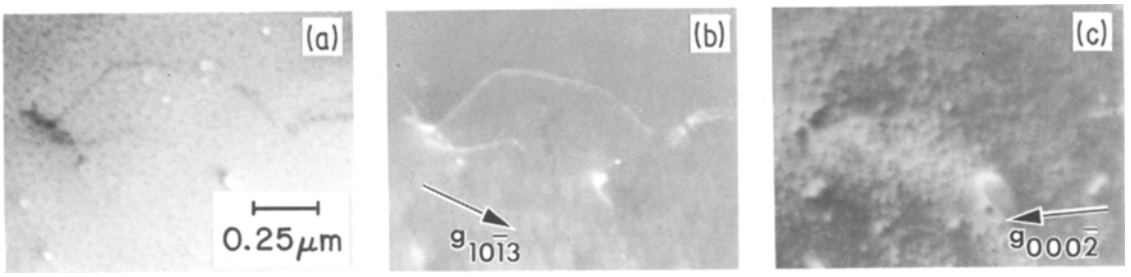

Figure 7 (a) Bright-field micrograph of dislocations in ice. Film orientation: [1 $\bar{2}$ 1 0]. (b) (1 0 $\bar{1}$ 3) dark-field image of Fig. 7a. Dislocations remaining visible proves that $\mathbf{g} \cdot \mathbf{b} \neq 0$. (c) Dislocation lines disappearing in this (0 0 0 $\bar{2}$) dark-field image indicates that the Burger's vector of the defects does not have a component along the *c* axis.

(Fig. 8). Jones [43] previously imaged dislocation loops in ice with X-ray topography. He found prismatic loops, with Burger's vectors lying along the hexagonal axis. The loops shown in Fig. 8, however, do not appear to be prismatic loops. Defects with c[0 0 0 1] Burger's vectors would be at least partially absent in the (0 $\bar{1}$ 1 0) dark-field image of Fig. 8b. Instead, the dislocation loops are almost invisible in the (1 0 $\bar{1}$ 1) dark-field image (Fig. 8c).

The data represented by Fig. 8 suggest that there are dislocation loops other than prismatic loops in ice. These loops may still lie in the basal plane but cannot have a c[0 0 0 1] Burger's vector. $\mathbf{b} = a/3$ [$\bar{2}$ 1 1 0] is also ruled out, as a defect with this displacement vector would be visible in Fig. 8c. A Burger's vector of $a/3$ [1 $\bar{2}$ 1 0] is consistent with the images in Fig. 8. For this assignment, $\mathbf{g} \cdot \mathbf{b} = 1$ in the (0 $\bar{1}$ 1 0) dark-field image and $\mathbf{g} \cdot \mathbf{b} = 0$ in the (1 0 $\bar{1}$ 1) dark-field image. Hence the system in Fig. 8 is apt to be [1 $\bar{2}$ 1 0] (0 0 0 1).

More common than isolated, simple dislocations in fast-frozen water layers are dislocation entanglements and pile-ups exemplified by Fig. 9. These complex defect structures can arise from stresses imposed on the film during solidifcation or transfer into the cold-stage.

4.2.4. *Images of stacking faults*

Fig. 10 shows stacking fault fringes which terminate at a low-angle tilt boundary in a wedge-shaped crystal of pure ice. The slip plane is identified as (1 0 $\bar{1}$ $\bar{1}$) from the angle it makes with the plane parallel to the sample surface. The angle is measured as $\tan^{-1}$ [($\xi_{11\bar{2}0}$ = 130 nm)/50 nm] = 69°, which compares well with the calculated angle of 62°. The slip direction is assigned as [$\bar{1}$ 2 $\bar{1}$ 0], which is a close-packed direction on

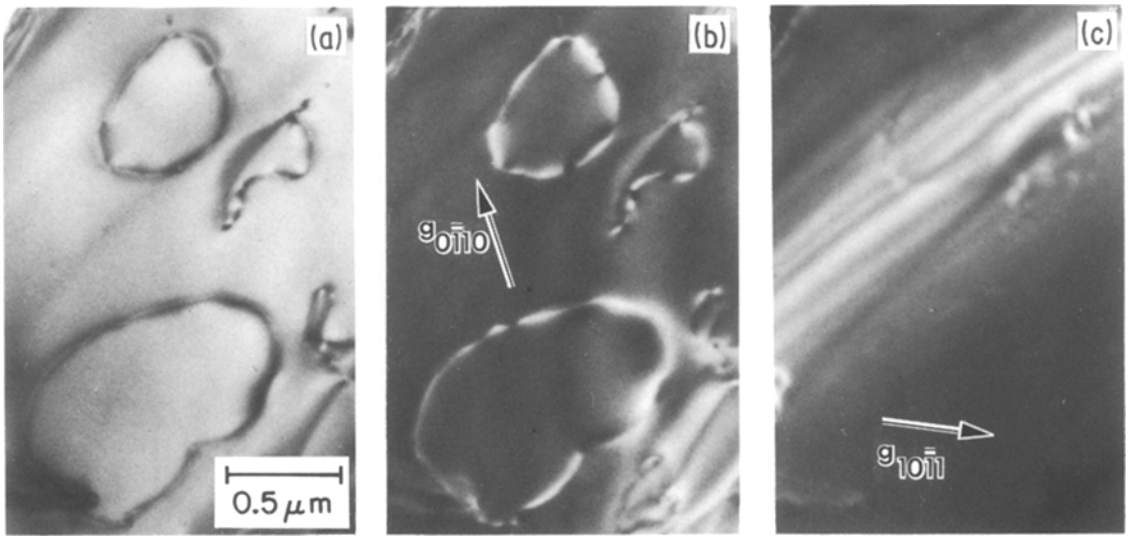

Figure 8 (a) Bright-field micrograph of dislocation loops in ice. Film orientation: [$\bar{2}$ 1 1 3]. (b) (0 $\bar{1}$ 1 0) dark-field image of area in (a). (c) (1 0 $\bar{1}$ 1) dark-field image in which the dislocation loops vanish.

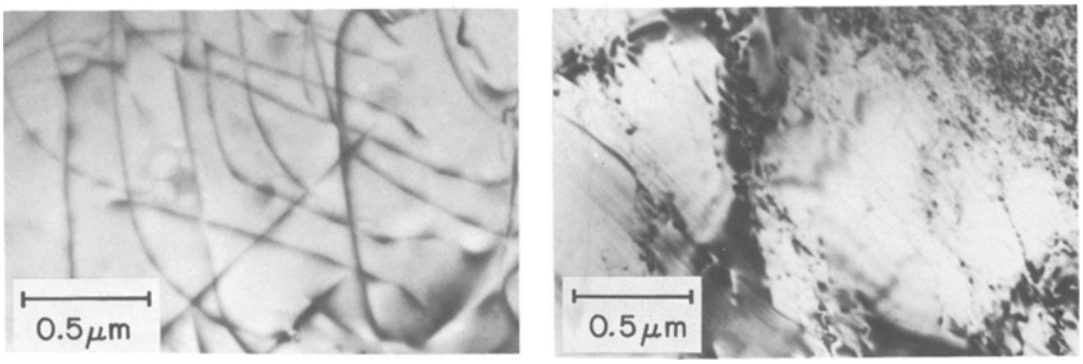

Figure 9 Bright-field micrographs showing dislocation networks in hexagonal ice.

$(1\,0\,\bar{1}\,\bar{1})$. $[\bar{1}\,2\,\bar{1}\,0]$ is also the direction of the contrast fringes in Fig. 10. The $(1\,0\,\bar{1}\,\bar{1})[\bar{1}\,2\,\bar{1}\,0]$ slip system cannot be detected by an etch-replication procedure [9].

The low-angle tilt boundary in Fig. 10 is identified from the slight displacement in thickness contours across it. Dislocations reside along this boundary. The regular distance between them is related to the displacement angle across the grain boundary through $\theta \simeq |\mathbf{b}|/d$, where θ is the angle of rotation at the boundary, $\mathbf{b}$ the Burger's vector of the dislocations at the boundary, and d the spacing between dislocations [45]. Because the spacing between the dislocations in Fig. 10 is approximately 25 nm and $|\mathbf{b}|$ is at most several tenths of nanometres (Table II), $\theta < 1°$.

5. Morphology of dilute solutions in ice

The structure of grains and grain boundaries in frozen, dilute aqueous solutions or dispersions of salts, surfactants, and polymers is akin to that in pure ice. Moreover, crystal lattice defects similar to those in pure hexagonal ice occur in frozen solutions. Figs. 11a and b show stacking fault fringes in frozen samples of 1 wt% aqueous SHBS and 0.4 wt% NaCl brine, respectively. Frozen dilute solutions usually contain more defects than pure ice does.

Hydrated, ionic crystals can precipitate from freezing samples of aqueous uranyl acetate, sodium chloride, or cesium chloride solutions. Fig. 12 is an example from a 0.4 wt% NaCl solution. In Fig. 12a, the particles appear dark against the ice in which they are embedded. Some of the precipitates are encased within ice crystals (A): at other places (B), they reside at grain boundaries.

When the specimen is tilted (Fig. 12b), bands of contrast can appear in the ice around some of the precipitates (C). Similar contours sometimes surround polystyrene spheres (Fig. 13a) and small liquid crystallites (Fig. 13b) in ice. The contrast bands are sensitive to tilt and can display lines along which there is no contrast (e.g. at (D) in Fig. 12b) [46]. They are therefore likely to be caused by strain fields created by differential expansion of ice and inclusions when samples solidify. When they occur, contrast bands prove that particles are indeed embedded within ice.

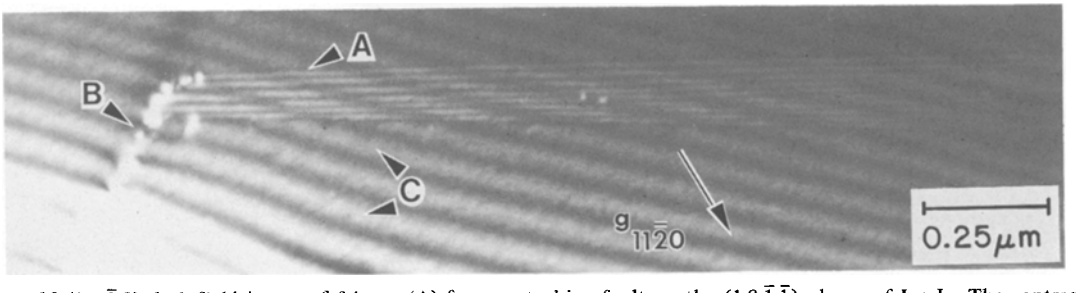

Figure 10 $(1\,1\,\bar{2}\,0)$ dark-field image of fringes (A) from a stacking fault on the $(1\,0\,\bar{1}\,\bar{1})$ planes of Ice I_h. The contrast fringes (A) terminate at a low-angle tilt boundary (B). The ice crystal is wedge-shaped, as evidenced by thickness fringes (C).

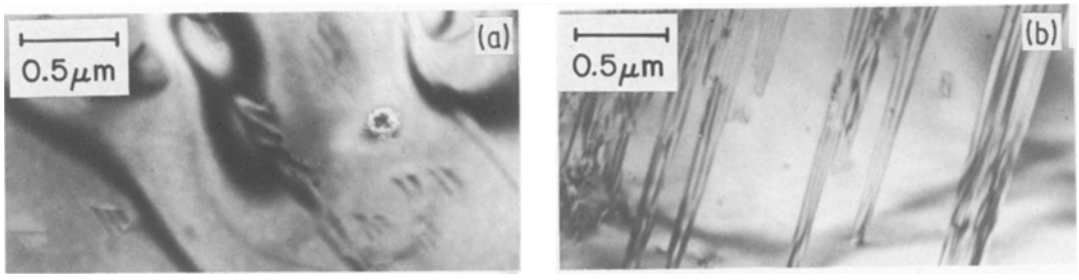

Figure 11 (a) Stacking fault fringes in a frozen, 1 wt % aqueous dispersion of SHBS. (b) Bright-field micrograph of fringes from stacking faults in frozen 0.4 wt % NaCl brine.

6. Summary

The nature of available cold-stage equipment and electron-beam radiolysis hampers electron microscopy of frozen, hydrated systems. With the fast-freeze, cold-stage microscopy system developed by Talmon *et al.* [1], however, useful information about the low temperature forms of ice can be obtained. Here the structure of grains and grain boundaries in thin, fast-frozen layers of aqueous samples has been studied. So far, basal and nonbasal dislocations, dislocation loops, and stacking faults in hexagonal ice have been imaged and identified. Although much remains to be done in indexing ice defects, the work here opens the way to using cold-stage microscopy to study defects in ice. Knowledge of the morphology of hexagonal ice is important in a myriad of scientific fields and technologies, including interpretation of the images of frozen, unstained, water-containing fluid microstructures [1–5].

Acknowledgements

This work was supported by the United States Department of Energy, the University of Minnesota Electron Microscopy Center, and the United States–Israel Binational Science Foundation (Jerusalem). We thank W. Adams of the Materials Lab at Wright–Patterson Air Force Base, Ohio, for providing the microdensitometer profiles in Fig. 1. We are also grateful to Professors H. T. Davis, L. E. Scriven and F. Franks for helpful comments on the manuscript.

References

1. Y. TALMON, H. T. DAVIS, L. E. SCRIVEN and E. L. THOMAS, *Rev. Sci. Instrum.* **50** (1979) 698.
2. *Idem*, in "Proceedings of the Seventh European Congress on Electron Microscopy", Vol. 2, edited by P. Brederoo and W. de Priester (Seventh European Congress on Electron Microscopy Foundation, Leiden, 1982) p. 718.
3. P. K. KILPATRICK, F. D. BLUM, H. T. DAVIS, A. H. FALLS, E. W. KALER, W. G. MILLER, J. E. PUIG, L. E. SCRIVEN, Y. TALMON and N. A. WOODBURY, in "Microemulsions", edited by I. D. Robb (Plenum Press, New York, 1982) p. 143.
4. E. W. KALER, A. H. FALLS, H. T. DAVIS, L. E. SCRIVEN and W. G. MILLER, *J. Colloid Interf. Sci.* **90** (1982) 424.
5. A. H. FALLS, H. T. DAVIS, L. E. SCRIVEN and Y. TALMON, *Biochem. Biophys. Acta* **693** (1982) 364.
6. J. D. CROSS, *Science* **164** (1969) 174.
7. J. D. CROSS, in "Physics of Ice", edited by N. Riehl, B. Bullemer, and H. Engelhardt (Plenum Press, New York, 1969) p. 81.

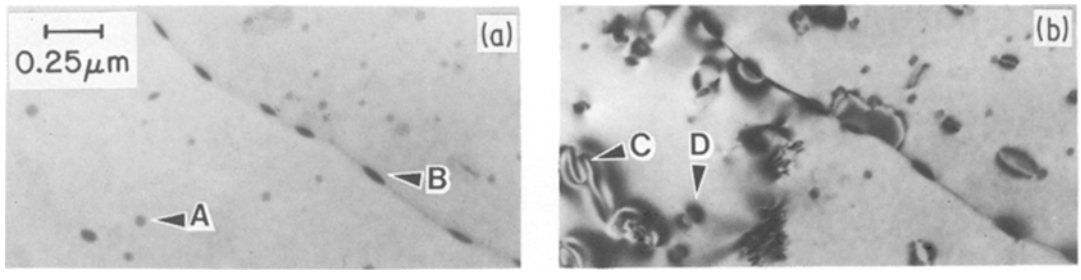

Figure 12 (a) Bright-field image of a frozen, 0.4 wt % NaCl brine solution. During freezing of the sample, NaCl crystals precipitate and eventually come to reside within ice grains (A) or at grain boundaries (B). (b) Area in Fig. 12a tilted by 1°. Precipitates induce strain fields in the ice matrix that produce bands of contrast (C) in the image. Some contours have a line of no contrast (D).

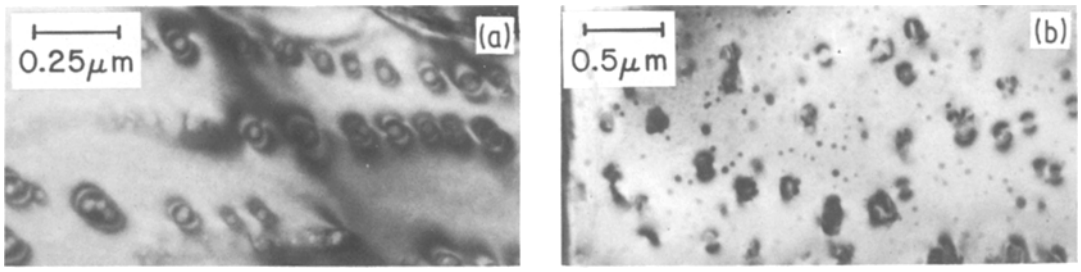

Figure 13 (a) Micrograph of a frozen, aqueous suspension of 1 wt % polystyrene spheres. The average sphere diameter is ~ 10 nm. The spheres induce strain fields in the ice around them. (b) Bright-field image of a 1 wt % dispersion of SHBS. The latter was vigorously shaken prior to freezing. Contours from strain fields surround small liquid crystallites.

8. N. K. SINHA, *Phil. Mag.* [Ser. 8] **36** (1977) 1385.
9. N. H. FLETCHER, "The Chemical Physics of Ice" (University Press, Cambridge, 1970) p. 25, 196.
10. V. N. VERTSNER and Gl. S. ZHDANOV, *Sov. Phys. Crystallogr.* **10** (1966) 597.
11. J. DUBOCHET, J. LEPAULT, R. FREEMAN, J. A. BERRIMAN and J.-C. HOMO, *J. Microsc.* **128** (1982) 219.
12. K. A. TAYLOR and R. M. GLAESER, *J. Ultrastructure Res.* **55** (1976) 448.
13. T. E. HUTCHINSON, D. E. JOHNSON and A. P. MacKENZIE, *Ultramicroscopy* **3** (1978) 315.
14. A. P. MacKENZIE and B. J. LUYET, in "Proceedings of the Fifth International Congress for Electron Microscopy", Vol. 2, edited by S. S. Breese (Academic Press, New York, 1962) p. P2.
15. J. DUBOCHET and A. W. McDOWALL, *J. Microsc.* **124** (1981) RP3.
16. P. N. T. UNWIN and J. MUGURUMA, *J. Appl. Phys.* **42** (1971) 3640.
17. *Idem, Phys. Status Solidi (a)* **14** (1972) 207.
18. E. I. FRANSES, PhD thesis, University of Minnesota (1979).
19. G. PERLOV, Y. TALMON and A. H. FALLS, *Ultramicroscopy* (1983) in press.
20. Y. TALMON and E. L. THOMAS, *J. Microsc.* **111** (1977) 151.
21. *Idem, ibid.* **113** (1978) 69.
22. N. H. FLETCHER, *Rep. Prog. Phys.* **34** (1971) 913.
23. P. V. HOBBS, "Ice Physics" (Clarendon Press, Oxford, 1974).
24. J. F. NICHOLAS, *Acta Crystallogr.* **21** (1966) 880.
25. H. KÖNIG, *Z. Kristallogr.* **105** (1943) 279.
26. G. HONJO, N. KITAMURA, K. SHIMAOKA and K. MIHAMA, *J. Phys. Soc. Jpn.* **11** (1956) 527.
27. N. D. LISGARTEN and M. BLACKMAN, *Nature* **178** (1956) 39.
28. H. FERNÁNDEZ-MORÁN, *Ann. New York Acad. Sci.* **85** (1960) 689.
29. V. F. DVORYANKIN, *Sov. Phys. Crystallogr.* **4** (1960) 415.
30. V. F. SHALLCROSS and G. B. CARPENTER, *J. Chem. Phys.* **26** (1957) 782.
31. L. G. DOWELL and A. P. RINFRET, *Nature* **188** (1960) 1144.
32. M. SUGISAKI, H. SUGA and S. SEKI, *Bull. Chem. Soc. Jpn.* **41** (1968) 2591.
33. E. F. BURTON and W. F. OLIVER, *Nature* **135** (1935) 505.
34. *Idem, Proc. Roy. Soc. Lond. A* **153** (1936) 166.
35. P. BRÜGGELLER and E. MAYER, *Nature* **288** (1980) 569.
36. E. MAYER and P. BRÜGGELLER, *ibid.* **298** (1982) 715.
37. R. BUSCALL and R. H. OTTEWILL, in "Specialist Periodical Report, Colloid Science", Vol. 2, edited by D. H. Everett (The Chemical Society, London, 1975) p. 191.
38. G. F. TELETZKE, private communication (1982).
39. G. THOMAS and M. J. GORINGE, "Transmission Electron Microscopy of Materials" (Wiley, New York, 1979) p. 38, 142, 172.
40. W. R. TYSON, *Can. J. Phys.* **49** (1971) 2181.
41. W. W. WEBB and C. E. HAYES, *Phil. Mag.* [Ser. 8] **16** (1967) 909.
42. A. FUKUDA and A. HIGASHI, in "Physics of Ice", edited by N. Riehl, B. Bullemer and H. Englehardt (Plenum Press, New York, 1969) p. 239.
43. S. J. JONES, *J. Appl. Phys.* **41** (1970) 2738.
44. P. R. SWANN, private communication; cold-stage instrumentation on display from Gatan, Inc. (Warrendale, PA) at the Fortieth Annual Meeting of the Electron Microscopy Society of America, 9–13 August 1982, Washington DC.
45. D. HULL, "Introduction to Dislocations" (Pergamon Press, Oxford, 1975) p. 201.
46. M. F. ASHBY and L. M. BROWN, *Phil. Mag.* [Ser. 8] **8** (1963) 1649.
47. F. FRANKS, *Cryoletters* **2** (1981) 69.

Received 2 November 1982
and accepted 4 February 1983